# AIAA 2000-3598

Computational Investigation of the Aerodynamic Effects on Fluidic Thrust Vectoring

K. A. Deere
NASA Langley Research Center
Hampton, VA

$M = 0.05$ NPR $= 5.2$ $\delta_p = -14.7°$

$M = 0.7$ NPR $= 5.2$ $\delta_p = -11.8°$
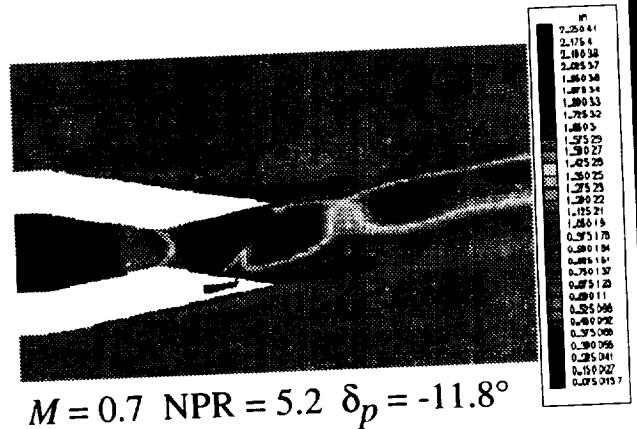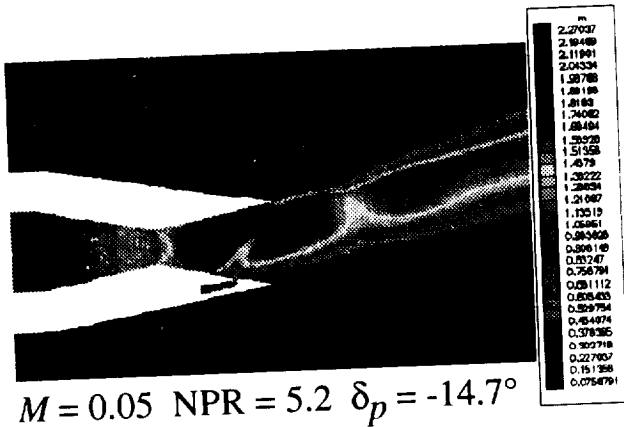
36th AIAA/ASME/SAE/ASEE
Joint Propulsion Conference & Exhibit
July 17-19, 2000 / Huntsville, AL

COMPUTATIONAL INVESTIGATION OF THE AERODYNAMIC EFFECTS ON FLUIDIC THRUST VECTORING

Karen A. Deere†
NASA Langley Research Center
Hampton, VA

ABSTRACT

A computational investigation of the aerodynamic effects on fluidic thrust vectoring has been conducted. Three-dimensional simulations of a two-dimensional, convergent-divergent (2DCD) nozzle with fluidic injection for pitch vector control were run with the computational fluid dynamics code PAB using turbulence closure and linear Reynolds stress modeling. Simulations were computed with static freestream conditions (M=0.05) and at Mach numbers from M=0.3 to 1.2, with scheduled nozzle pressure ratios (from 3.6 to 7.2) and secondary to primary total pressure ratios of $p_{t,s}/p_{t,p}$=0.6 and 1.0. Results indicate that the freestream flow decreases vectoring performance and thrust efficiency compared with static (wind-off) conditions. The aerodynamic penalty to thrust vector angle ranged from 1.5 degrees at a nozzle pressure ratio of 6 with M=0.9 freestream conditions to 2.9 degrees at a nozzle pressure ratio of 5.2 with M=0.7 freestream conditions, compared to the same nozzle pressure ratios with static freestream conditions. The aerodynamic penalty to thrust ratio decreased from 4 percent to 0.8 percent as nozzle pressure ratio increased from 3.6 to 7.2. As expected, the freestream flow had little influence on discharge coefficient.

INTRODUCTION

There are a host of potential benefits for incorporating thrust vectoring into military aircraft: enhanced turn rate, improved maneuverability, vertical and short take-off and landing (V/STOL) capabilities, and elimination of control surfaces, to name a few. Eliminating conventional control surfaces in lieu of propulsive controls may result in weight, signature, and drag reductions. The use of fluidic injection for thrust vectoring, instead of mechanized hardware, offers further improvements in aircraft signature, weight, and drag.

The thrust vectoring studies initiated in the 1960's included gimbal and swivel mechanisms added to the tailpipe, prior to the axisymmetric nozzle, to improve take-off and landing performance (refs. 1-3). These mechanisms proved efficient for thrust vectoring under

static conditions, but resulted in detrimental penalties for installed conditions.

The studies throughout the 1970's investigated a variety of non-axisymmetric nozzles: such as two-dimensional convergent-divergent (2DCD), wedge, and single-expansion-ramp nozzles (SERN), for their ability to accommodate thrust vectoring (refs. 1-10). Non-axisymmetric, thrust-vectoring nozzles offered integration and installed performance benefits over the conventional axisymmetric nozzles (ref. 11).

Mechanical, multiaxis thrust vectoring was investigated in the 1980's. Augmenting conventional controls with pitch and yaw propulsive control allowed for supermaneuverability or operation in the post-stall regime, where conventional controls are ineffective (refs. 12-13). Pitch and yaw vectoring was accomplished primarily with deflection of the divergent flaps, but integration concepts and post-exit vanes were also investigated (refs. 14-18). Most concepts that vectored the flow with subsonic turning achieved the best vectoring effectiveness and incurred the least thrust performance penalties. Installed performance of mechanical multiaxis thrust vectoring nozzles was shown to be mostly independent of angle-of-attack and sideslip angle (ref. 19), unlike conventional aerodynamic control surfaces.

---

†Aerospace Engineer, Configuration Aerodynamics Branch, Aerodynamics Competency. Member AIAA

Fluidic injection for thrust vectoring was investigated in the 1990's (ref. 20-26). Instead of deflections of divergent flaps or vanes to create pressure differentials and vectored thrust, fluidic thrust vectoring introduces a secondary air stream into the primary jet flow to create an off-axis deflection of the jet thrust. Two of the most mature fluidic techniques are throat skewing and shock vector control. However, some less mature concepts like counterflow (ref. 25-26) and synthetic jets (ref. 27) have also been introduced for thrust vectoring. Throat skewing was built on the database of mechanical concepts that demonstrated the efficiency of turning the flow subsonically. Fluidic injection occurs near the throat of the nozzle to shift the sonic line, turn the flow subsonically, and create an asymmetric pressure loading in the throat-skewing concept. For the shock vector control technique, the secondary air stream is introduced in the divergent portion of the nozzle and hence, affects supersonic flow. Similar to the mechanical concepts that turn the flow supersonically, the shock vector control technique has more thrust losses associated with it, but in general, substantial vector angles can be achieved. In addition, fluidic thrust vectoring is generally more effective at overexpanded nozzle pressure ratios. To date, most of the data on fluidic thrust vectoring has been obtained at static freestream conditions (refs. 20-26). Unlike mechanical thrust vectoring, there is very little, if any, data documenting the effects of the freestream flow on thrust vectoring with fluidic injection.

The current investigation attempted to initiate a database of external flow effects on fluidic thrust vectoring. The nozzle under investigation was a two-dimensional, convergent-divergent (2DCD) nozzle with fluidic injection for pitch thrust vector control. The secondary air stream was injected through a slot in the lower divergent wall. Computational fluid dynamics (CFD) was used to simulate the nozzle at typical nozzle pressure ratio (NPR) schedule based on Mach number, up to $M=1.2$. Simulations were also computed at the same NPR schedule with static freestream conditions ($M=0.05$) to document the effect of the external freestream on vectoring effectiveness, thrust efficiency, and discharge coefficient. Secondary to primary total pressure ratios of 0.6 and 1.0 were investigated, which corresponded to secondary weight flow rates of 5.8 percent and 9.65 percent of the primary weight flow rate, respectively.

COMPUTATIONAL METHOD

Governing Equations

The PAB computer code solves the three-dimensional, Reynolds-averaged Navier-Stokes (RANS) equations and uses one of several turbulence models for closure of the RANS equations. The governing equations are written in generalized coordinates and in conservative form. In an effort to decrease computational resources, the simplified, thin-layer Navier-Stokes equations are implemented into PAB. This approximation neglects derivatives in the viscous terms streamwise and parallel to the surface, since they are typically negligible in comparison to the derivatives normal to the surface. Extensive details of PAB are found in references 28 and 29.

The flow solver was written with three numerical schemes: the flux vector-splitting scheme of van Leer (ref. 30), the flux difference-splitting scheme of Roe (ref. 31), and a modified Roe scheme primarily used for space marching solutions. These schemes implement the finite volume principle to balance the fluxes across grid cells and the upwind biased scheme of van Leer or Roe to determine fluxes at the cell interfaces. Only the inviscid terms of the flux vectors are split and upwind differenced, while the diffusion terms of the Navier-Stokes equations are centrally differenced. The details and applications of these methods are given in references 29-31.

For this study and other typical three-dimensional simulations, the solutions are computed with the van Leer and Roe schemes. An iteration to steady state in a three-dimensional computational domain includes a forward and backward relaxation sweep in the streamwise direction, while implicitly updating each cross plane.

Turbulence Modeling

Turbulence modeling is required to predict solutions for many flow fields. The PAB code can perform several turbulence simulations by implementing either an algebraic or 2-equation, linear or nonlinear turbulence model. An algebraic 2-layer, Baldwin-Lomax model is accurate for simple viscous flows because the turbulent viscosity μ_T is determined by a local function. A 2-equation k-ε model with second order closure is used to model more complex viscous flow features. A second equation is used to solve for the turbulent length scale in addition to the equation for turbulent kinetic energy (k). Since the k-ε model has a singularity at solid surfaces, either a damping function or a wall function must be implemented to adjust the turbulent viscosity (ε) near

these surfaces. The grid in the boundary layer at wall surfaces must be well defined with a law-of-the-wall coordinate (y^+) of approximately 2 for adequate modeling of the boundary layer flow (ref. 32). The restriction on y^+ may be relaxed to 50 if a wall function is implemented. However, it is customary to restrict the use of wall functions to attached flows.

Both linear and nonlinear turbulence simulations use the standard model coefficients of the k-e equations as a basis of formulation. The linear k-ε turbulence model is an eddy viscosity model with the following formulation for τ:

$$\tau_{ij} = \tau_{ij}^L + \tau_{ij}^T \qquad (1)$$

where,

$$\tau_{ij}^L = \frac{2}{3}\mu_L S_{kk}\delta_{ij} - 2\mu_L S_{ij} \qquad (2)$$

$$\tau_{ij}^T = \frac{2}{3}(\rho k + \mu_T S_{kk})\delta_{ij} - 2\mu_T S_{ij} \qquad (3)$$

$$S_{ij} = \frac{1}{2}(\frac{\partial u_i}{\partial x_j} + \frac{\partial u_j}{\partial x_i}) \qquad (4)$$

$$\mu_T = f_\mu C_\mu \frac{k^2}{\varepsilon} \qquad (5)$$

The damping function, f_μ, is an empirical function, while C_μ is set to 0.09 for the standard linear k-ε turbulence model. The turbulence model has one equation for turbulent kinetic energy, k, and one for turbulent energy dissipation, ε. The k and ε pair of coupled transport equations are written in conservative form which can be uncoupled from the Navier-Stokes equations and from each other to decrease computational requirements. In an effort to decrease numerical stiffness, the k and ε equations are solved at approximately 25 percent of the Courant-Friedrichs-Levy (CFL) number for the Navier-Stokes equations.

The PAB code, with 2-equation, linear Reynolds stress modeling, was chosen for these simulations because this code was developed for and can accurately predict propulsive flows with mixing, separated flow regions, and jet shear layers. A modified Jones and Launder form (ref. 33) of the damping function (f_μ) was utilized to treat the singularity at the wall. A high Reynolds number model with no damping function was implemented in the free stream blocks.

Performance Calculation

The PAB code contains a performance module (ref. 34) that utilizes the momentum theorem applied to a user-defined control volume to calculate nozzle or aerodynamic performance. Quantities such as lift, drag, thrust, moments, heat transfer, and skin friction

may be computed for many complex geometric configurations and multi-stream flows. Each quantity is updated throughout the solution development to monitor convergence.

Along flow-through sections of the control volume, mass and momentum fluxes, as well as pressure forces are integrated over each cell with equations 6 and 7.

$$w_p = \Sigma \ \{\rho U \cdot N\} \ \Delta A \qquad (6)$$

$$F_{flux} = \Sigma \ \{\rho U \ (U \cdot N) \ + \ (p - p_\infty)N\}\Delta A \qquad (7)$$

where ΔA is the cell face area and N is the cell face unit vector.

Along solid surfaces of the control volume, skin friction and pressure forces are determined. Surface pressure force $F_{pressure}$ is determined by multiplying cell static pressure by cell face area using equation 8.

$$F_{pressure} = \Sigma \ [(p - p_\infty)N]\Delta A \qquad (8)$$

The cell surface static pressure is calculated by extrapolating the cell centered static pressure to the surface where the velocity is assumed to be zero.

The skin friction force $F_{friction}$ is calculated with only the velocity gradients normal to the surface contributing to the velocity terms of the viscous stress tensor. A two-point difference is used to determine a velocity gradient, one zero-magnitude velocity vector at the surface and a second at the cell center. Sutherland's formula (ref. 35) is used to calculate the dynamic viscosity at the surface by extrapolating the static temperature at a local cell center to the surface and using a reference viscosity and temperature condition. The total body force vector F is defined in equation 9.

$$F = F_{flux} + F_{pressure} + F_{friction} \qquad (9)$$

Boundary Conditions

The PAB code has many options for defining the conditions of the inflow, outflow, free stream, wall, and centerline boundaries. For this study, Riemann invariants along the characteristics were implemented along the lateral and in-flow free stream boundaries. A first order extrapolation outflow condition was used at the downstream far field boundary. The primary nozzle flow and the secondary fluidic injection flow were specified with a fixed total temperature and total pressure boundary condition. A no-slip adiabatic wall boundary condition was implemented to obtain viscous solutions.

Nozzle Geometry

The two-dimensional, convergent-divergent (2DCD) fluidic thrust-vectoring nozzle was installed in an isolated nacelle to investigate the interaction between the external freestream flow and the nozzle exhaust flow. An isometric view of the isolated nacelle mounted on a strut is shown in figure 1. The length of the isolated nacelle is 64.745 inches. The nozzle had a length of 8 inches, a throat area of A_t=5.416 in^2, an expansion ratio of A_e/A_t=2.4, and an injection slot area of $A_{t,slot}$=0.565 in^2. The design nozzle pressure ratio and exit Mach number, based on one-dimensional theory, are NPR$_D$=14.588 and M=2.4, respectively.

Computational Domain

The computational mesh was fully three-dimensional with 2 blocks defining the internal nozzle, 1 block representing the injection plenum and 16 blocks representing the freestream domain. The internal blocking structure representing the nozzle and boattail is shown in Figure 2. The injection plenum, shown in Figure 3, had one-to-one grid matching with the nozzle divergent section mesh. A centerline cut of the isolated nacelle and nozzle is shown in Figure 4. The far field was located 10 body lengths upstream and downstream of the aerodynamic nose and nozzle exit, respectively. The upper and lower lateral far field was located 6 body lengths above and below the aerodynamic body. The boundary layer was defined for a law-of-the-wall coordinate y^+ of 0.5 on the fine mesh spacing for adequate modeling of the boundary layer flow.

RESULTS

Three-dimensional computational solutions were predicted with the Navier-Stokes code PAB using turbulence closure and linear Reynolds stress modeling. Baseline, or no-vectoring simulations were computed at nozzle pressure ratio (NPR) and freestream Mach numbers listed in Table 1. Vectoring simulations were computed with static freestream conditions (M=0.05) and with freestream Mach numbers of 0.3 to 1.2 at the NPRs listed in Table 1. In addition, two cases were computed at the design NPR$_D$=14.588 with M=0.3 and M=1.2 freestream conditions. Vectoring simulations were computed with secondary to primary total pressure ratios $(p_{t,s}/p_{t,p})$ of 0.6 and 1. The simulated conditions were chosen to coordinate with an experimental test matrix.

Baseline, No Vectoring Cases

Four simulations with no vectoring (no secondary fluidic injection) were completed at the nozzle pressure ratios and corresponding scheduled freestream Mach numbers listed in Table 1. Internal performance is shown in Table 2. Discharge coefficient is dependent on the geometry in the convergent section and the geometry immediately downstream of the geometric minimum area (nozzle throat) for CD nozzles. Therefore, once the nozzle is choked, generally at NPR<2, discharge coefficient will reach a constant value. For the no vectoring cases, primary flow discharge coefficient $(C_{d,p})$ was relatively constant over the range of NPR. The boundary layer in the M=0.7 and NPR=5.2 case was slightly thicker than the other three cases, resulting in a 0.25 percent lower discharge coefficient.

Thrust ratio $(C_{f,g})$ increased nearly 8.5 percent as NPR increased from 3.6 to 7.2. At overexpanded conditions (NPR<NPR$_D$), losses due to shocks and separated flow inside the nozzle are significant. As the flow conditions approach the design NPR, the shock moves downstream in the nozzle and thrust approaches ideal. At fully expanded conditions, the nozzle is internally shock-free and losses from ideal thrust primarily include skin friction and flow angularity (due to nozzle divergence).

There was a small pitch vector angle, δ_p<0.4, for the cases with no secondary injection, see Table 2. The slot was included in the computational domain for the no injection simulations and left "open" to the primary nozzle. Therefore, small differences between the static pressures along the upper and lower wall existed (see figure 5(a)), and resulted in small non-zero pitch vector angles for the no injection cases.

Mach contours and normalized internal static pressures along the nozzle centerline are shown in figures 5 through 8 for NPRs=3.6, 5.2, 6, and 7.2 at the scheduled Mach numbers, with no secondary injection. The pressure dropped in the convergent section of the nozzle (x<39.9 inches) as the subsonic flow accelerated to M=1 at the throat (x=39.9 inches). The pressure increased at the throat as the flow negotiated through the sudden change in geometry from the convergent section to the divergent section of the nozzle (x>39.9 inches). As the flow accelerated to supersonic conditions in the divergent section of the nozzle, the pressure continued to drop. At these overexpanded conditions (NPR<14.588), the pressure dropped below ambient pressure in the divergent section, but was adjusted to ambient conditions through a series of oblique shocks. At NPR=3.6 with M=0.3

freestream flow conditions, the shock was located at x=42 inches, see figure 5(b). With no secondary fluidic injection, the pressures along the upper and lower wall were nearly identical, with the shocks located in the same axial location. The flow appears separated downstream of the shock, as evidenced by the relatively flat pressure distribution for x>42.2 inches. The shock and flow separation is shown in the Mach contours in figure 5(c), with the shock located just upstream of the injection slot. The reversed flow at the point of separation from the upper wall is shown with u-velocity vectors in figure 5(d). As NPR was increased, the flow expanded further along the nozzle wall before the flow adjusted through a shock, compare figures 5 - 8.

Effect of Freestream Flow on Pitch Vectoring

To understand the effects of the freestream flow on fluidic thrust vectoring, simulations were computed at nozzle pressure ratios of NPR=3.6, 5.2, 6, and 7.2 with static freestream conditions (M=0.05) and with the scheduled Mach numbers listed in Table 1. Internal performance for the simulations with static freestream conditions are shown in Table 3 and with the scheduled freestream Mach numbers are shown in Table 4. The ratio of secondary to primary total pressure was 0.6, resulting in a secondary injection flow rate of 5.8 percent of the primary flow rate.

The influence of the M=0.3 freestream flow acted to decrease vectoring effectiveness by increasing the negative pitch vector angle (δ_p) 2.8 degrees at NPR=3.6, compared to static freestream conditions. Figure 9 shows the internal, centerline pressure distributions for the NPR=3.6 cases with M=0.05 and M=0.3 freestream conditions. The shock on the upper wall moved further inside the nozzle, from x=42.5 inches to x=42.25 inches, creating a larger region of separated flow with the influence of the freestream flow, figure 9(a). The freestream flow only influenced the pressure along the lower surface downstream of the injection slot, see figure 9(b). The pressure distributions along the wall downstream of the injection slot, were both at lower static pressures than ambient conditions. However, the M=0.3 freestream flow case had a greater suction force on the wall for x>42.2 inches, than the static freestream flow case. The combined effect of moving the shock upstream on the upper wall and increased suction on the lower wall resulted in a reduction of thrust vector effectiveness with a freestream flow of M=0.3.

Figures 10(a) and 10(b) show the Mach contours along the nozzle centerline for the NPR=3.6 cases at M=0.3 and M=0.05, respectively. The larger region of separated flow along the upper wall with wind-on

conditions (*M*=0.3 freestream flow) is evident in the Mach contours. In addition, the shock cells in the plume dissipated faster at *M*=0.3 conditions than at static conditions. The Mach number reached *M*=1.6 in the first shock cell of the external plume with static freestream conditions, but only reached *M*=1.4 with wind-on freestream conditions.

The influence of *M*=0.7 freestream conditions also acted to decrease thrust vector effectiveness, with an increase in negative pitch vector angle of 2.9 degrees at NPR=5.2, compared to static freestream conditions. Figure 11 shows the effect of freestream flow on internal, centerline pressure distributions for the NPR=5.2 cases with *M*=0.05 and *M*=0.7 freestream conditions. The freestream flow had the same effects on the pressure distributions that it had at NPR=3.6. The shock on the upper wall moved further inside the nozzle and a greater suction force was created on the lower wall, downstream of the injection slot with the influence of the freestream flow. The Mach contours for the NPR=5.2 cases are shown in figure 12. A shock formed and the flow separated from the upper wall with *M*=0.7 freestream flow, figure 12(a), but the flow remained attached to the upper wall until the nozzle exit for the static freestream case.

Trends similar to the NPR<6 cases are seen for the NPR=6 cases, see figures 13 and 14. However, at NPR=6, the suction on the lower wall, downstream of the injection slot is not as great as for the NPR<6 cases (figure 13). Therefore, the penalty in pitch thrust vector angle due to wind-on conditions is less than for the NPR<6 cases, 1.5 degrees compared to approximately 2.9 degrees.

The wind-on (*M*=1.2) penalty to pitch thrust vector angle for the NPR=7.2 case was 2.2 degrees. Figure 15 shows the internal, centerline pressure distributions for the NPR=7.2 cases with *M*=0.05 and *M*=1.2 freestream conditions. There is little difference in pressures along the upper wall because the flow remained attached until the exit, figure 15(a). However, as with the NPR<6 cases, the suction on the lower wall downstream of the injection slot is much greater than the NPR=6 case, resulting in a greater penalty to thrust vector angle. The Mach contours along the nozzle centerline for the NPR=7.2 cases are shown in figure 16.

Figure 17 shows the effect of freestream flow on system thrust ratio, $C_{f,g,sys}$. Thrust ratio was decreased 4.1 percent at NPR=3.6 and 0.83 percent at NPR=7.2 with the influence of the freestream flow. As expected, the largest thrust penalty occurred at the most overexpanded condition. The further off design (overexpanded conditions) the nozzle, the more the internal flow separated from the divergent walls. The

freestream flow influenced the separated, subsonic flow inside the nozzle, which pushed the shock further upstream and separated even more flow from the divergent walls. Although a thrust improvement is sometimes realized from shock induced separation, which effectively changes the expansion ratio to a more suitable one for a set of conditions, thrust was penalized in these cases. Loss of flow expansion along the walls, less flow momentum at the nozzle exit, and greater total pressure losses from shocks in the nozzle could explain the loss in thrust with the influence of the freestream flow.

As expected, the freestream flow had minimal influence on internal nozzle discharge coefficient, see figure 18. Again, discharge coefficient is dependent on the geometry in the convergent section and the geometry immediately downstream of the throat. For these cases, the influence of the external flow remained in the divergent portion of the nozzle causing little impact on discharge coefficient.

Effect of NPR on Pitch Vectoring

Two simulations were completed to document the effect of NPR on pitch thrust vectoring at freestream Mach numbers of *M*=0.3 and *M*=1.2. The internal performance is shown in Table 5. Pitch thrust vectoring was achieved with a secondary to primary total pressure ratio of $p_{t,s}/p_{t,p}$=0.6. The secondary injection weight flow rate for $p_{t,s}/p_{t,p}$=0.6 was 5.8 percent of the primary weight flow rate.

At both Mach numbers, thrust ratio increased and pitch vector angle decreased with increasing NPR. In both cases, the shock on the upper wall moved outside of the nozzle from x=42.2 inches, while the shock and separation on the lower wall, upstream of the injection slot, also moved downstream as NPR increased, see figures 19 and 20. Eliminating the shock and separation along the upper wall improved thrust, but also decreased the pressure differential between the upper and lower surfaces that caused pitch thrust vectoring.

Effect of Secondary to Primary Total Pressure Ratio on Pitch Vectoring

The effect of secondary to primary total pressure ratio on internal performance is shown in Table 6. An additional simulation was computed at a nozzle pressure ratio of NPR=3.6 with *M*=0.3 freestream conditions and a secondary to primary total pressure ratio of 1. The secondary injection weight flow rate was 9.65 percent of the primary weight flow rate. At NPR=3.6, the effect of increasing total pressure of the secondary injection

stream had an adverse impact on thrust vector angle and thrust ratio.

In general, as injection flow rate increases from a no injection state, thrust vector angle also increases (ref. 20, 23). However, at a particular injection rate, thrust vector angle will peak, resulting in diminishing returns for any further increase in injection rate. In some cases, adverse effects such as shock impingement (ref. 23) or flow reattachment will cause a decrease in vectoring with increased injection flow rate.

In the case shown in Table 6, pitch thrust vectoring effectiveness decreased as secondary to primary total pressure ratio increased from 0.6 to 1. The centerline pressure distributions shown in figure 21 help to explain the penalty to pitch thrust vector angle. The shock and flow separation from the upper wall moved further upstream, but then also reattached to the upper wall near x=42.8 inches, as injection total pressure increased. The flow reattachment to the upper surface is shown in the comparison of Mach contours in figure 22. The shock in front of the injection slot on the lower wall moved further upstream as injection total pressure increased, see figure 21. The decreased pressure differential along the top and bottom wall resulted in a penalty of 3.38 degrees to pitch vector angle.

System thrust ratio decreased about 1 percent with $p_{t,s}/p_{t,p}$=0.6 (w_s=5.8 percent of w_p), but increased 0.65 percent with $p_{t,s}/p_{t,p}$=1 (w_s=9.65 percent of w_p), compared to the no injection case (w_s=0.01 percent of w_p), see Table 6. The flow reattachment to the upper wall in the $p_{t,s}/p_{t,p}$=1 case may have caused the thrust ratio improvement, but at a penalty to pitch vector angle. As expected, discharge coefficient was virtually unaffected by the increase of injection total pressure.

CONCLUSIONS

A computational study was completed on a fluidic pitch-vectoring, two-dimensional, convergent-divergent nozzle to document the effect of the external freestream flow on fluidic thrust vectoring effectiveness. The computational fluid dynamics code PAB was used with two-equation turbulence closure and linear Reynolds stress modeling.

The external freestream flow decreased fluidic thrust vectoring effectiveness by 1.5 to 2.9 degrees over the range of NPR and Mach number schedule. The freestream flow influenced the separated, subsonic, internal flow by moving the location of the upper-wall shock upstream and caused increased suction on the lower wall, downstream of the injection slot. The overall decrease in pressure differential between the

upper and lower walls resulted in less vectoring with wind-on conditions.

Thrust ratio was decreased 4.1 percent at NPR=3.6 and 0.83 percent at NPR=7.2 with the influence of the freestream flow. As expected, the largest thrust penalty occurred at the most overexpanded condition where internal flow separation was the greatest. In addition, the freestream flow increased internal flow separation by moving the shock further upstream along the upper wall. As a result, thrust was reduced from a possible combination of reduced flow expansion, reduced flow momentum at the nozzle exit, and increased total pressure losses.

The freestream flow had a minimal influence on nozzle discharge coefficient, as expected. The influence of the external flow was limited to subsonic flow in the divergent section of the nozzle, caused by separation at overexpanded conditions. Since discharge coefficient is dependent on the flow in the nozzle geometry up through the nozzle throat, discharge coefficient was not impacted by the external flow.

REFERENCES

1. Hiley, P. E.; Wallace, H. W.; and Booz, D. E.: *Nonaxisymmetric Nozzles Installed in Advanced Fighter Aircraft*. J. Aircraft, Vol. 13, No. 12, December 1976, pp. 1000-1006.

2. Willard, C. M.; Capone, F. J.; Konarski, M.; and Stevens, H.L.: *Static Performance of Vectoring/Reversing Nonaxisymmetric Nozzles*. AIAA 840, 1977.

3. Bergman, D.; Mace, J. L.; and Tayer, E. B.: *Nonaxisymmetric Nozzle Concepts for an F-111 Test Bed*. AIAA 841, 1977.

4. Stevens, H. L.: *F-15/Nonaxisymmetric Nozzle System Integration Study Support Program*. NASA CR-135252, 1978.

5. Maiden, D. L., and Petit, J.E.: *Investigation of Two-Dimensional Wedge Exhaust Nozzles for Advanced Aircraft*. AIAA 1317, 1975.

6. Capone, F. J.; and Maiden, D. L.: *Performance of Twin Two-Dimensional Wedge Exhaust Nozzles Including Thrust Vectoring and Reversing Effects at Speeds Up to Mach 2.2*. NASA TN D-8449, 1977.

7. Pendergraft, O. C. Jr.: *Comparison of Axisymmetric and Nonaxisymmetric Nozzles Installed on the F-15 Configuration*. AIAA 842, 1977.

8. Lander, J. A.; Nash, D. O., and Palcza, J. L.: *Augmented Deflector Exhaust Nozzle/ ADEN/ Design for Future Fighters.* AIAA 1318, 1975.

9. Goetz, G. F.; Young, J. H., and Palcza, J. L.: *A Two-Dimensional Airframe Integrated Nozzle Design with Inflight Thrust Vectoring and Reversing Capabilities for Advanced Fighter Aircraft.* AIAA 626, 1976.

10. Wasson, H. R.; and Hall, G. R.: *Results of a Feasibility Study to Add Canards and ADEN Nozzle to the YF-17.* AIAA 1227, 1977.

11. Berrier, B. L.; and Re, R. J.: *A Review of Thrust-Vectoring Schemes for Fighter Aircraft.* AIAA 78-1023, July 1978.

12. Herbst, W. B.: *Supermaneuverability.* Workshop on Unsteady Separated Flow, Michael S. Francis and Marvin W. Luttges, eds, AFOSR-TR-84-3109, U.S. Air Force, May 1984, pp. 1-9.

13. Gallaway, C. R.; and Osborn, R. F.: *Aerodynamics Perspective of Super-maneuverability.* AIAA 85-4068, October 1985.

14. Capone, F. J.; and Mason, M. L.: *Multiaxis Aircraft Control Power from Thrust Vectoring at High Angles of Attack.* NASA TM-87741, June 1986.

15. Berrier, B. L.; and Mason, M. L.: *Static Investigation of Post-Exit Vanes for Multiaxis Thrust Vectoring.* AIAA 87-1834, June-July 1987.

16. Capone, F. J.; and Bare, E. A.: *Multiaxis Control Power from Thrust Vectoring for a Supersonic Fighter Aircraft Model at Mach 0.2 to 2.47.* NASA TP-2712, July 1987.

17. Taylor, J. G.: *A Static Investigation of a Simultaneous Pitch and Yaw Thrust Vectoring 2-D C-D Nozzle.* AIAA 88-2998, July 1988.

18. Berrier, B. L.; and Mason, M. L.: *Static Performance of an Axisymmetric Nozzle with Post-Exit Vanes for Multiaxis Thrust Vectoring.* NASA TP-2800, May 1988.

19. Berrier, B. L.: *Results from NASA Langley Experimental Studies of Multiaxis Thrust Vectoring Nozzles.* SAE TP-881481, October 1988.

20. Chiarelli, C.; Johnsen, R. K.; and Shieh, C. F.: *Fluidic Scale Model Multi-Plane Thrust Vector Control Test Results.* AIAA 93-2433, June 1993.

21. Giuliano, V. J.; Flugstad T. H.; Semmes, R.; and Wing, D. J.: *Static Investigation and Computational Fluid Dynamics (CFD) Analysis of Flowpath Cross-Section and Trailing-Edge Shape Variations In Two Multiaxis Thrust Vectoring Nozzle Concepts.* AIAA 94-3367, June 1994.

22. Federspiel, J.; Bangert, L.; Wing, D.; and Hawkes, T.: *Fluidic Control of Nozzle Flow - Some Performance Measurements.* AIAA 95-2605, July 1995.

23. Anderson, C. J.; Giuliano, V. J.; and Wing, D. J.: *Investigation of Hybrid Fluidic/Mechanical Thrust Vectoring for Fixed-Exit Exhaust Nozzles.* AIAA 97-3148, July 1997.

24. Deere, K. A.: *PAB Simulations of a Nozzle with Fluidic Injection for Yaw Thrust-Vector Control.* AIAA 98-3254, July 1998.

25. Hunter, C. A.; and Deere, K. A.: *Computational Investigation of Fluidic Counterflow Thrust Vectoring.* AIAA 99-2669, June 1999.

26. Flamm, J. D.: *Experimental Study of a Nozzle Using Fluidic Counterflow for Thrust Vectoring.* AIAA 98-3255, July 1998.

27. Pack, L. G.; and Seifert, A.: *Periodic Excitation for Jet Vectoring and Enhanced Spreading.* AIAA 99-0672, January 1999.

28. Abdol-Hamid, Khaled, S.: *Implementation of Algebraic Stress Models in a General 3-D Navier-Stokes Method (PAB).* NASA CR-4702, 1995.

29. Abdol-Hamid, Khaled, S.: *Application of a Multiblock/Multizone Code (PAB) for the Three-Dimensional Navier-Stokes Equations.* AIAA-91-2155, June 1991.

30. van Leer, B.: *Flux-Vector Splitting for the Euler Equations.* ICASE Report 82-30, 1982.

31. Roe, P. L.: *Characteristics Based Schemes for the Euler Equations.* A Numerical Review of Fluid Mechanics, 1986, pp. 337-365.

32. Abdol-Hamid, Khaled S.; Lakshmanan, B.; and Carlson, John R.: *Application of Navier-Stokes Code PAB With k-ε Turbulence Model to Attached and Separated Flows.* NASA TP-3480, January 1995.

33. Jones, W. P.; and Launder, B. E.: *The Prediction of Laminarization With a Two-Equation Model of Turbulence.* Int. Journal of Heat & Mass Transfer, vol. 15, no. 2, February 1972, pp. 301-314.

34. Carlson, John R.: *A Nozzle Internal Performance Prediction Method.* NASA TP-3221, October 1992.

35. Ames Research Staff: *Equations, Tables, and Charts for Compressible Flow.* NACA Report 1135, 1953.

8

Scheduled Mach Number	NPR
0.3	3.6
0.7	5.2
0.9	6
1.2	7.2

Table 1. NPR schedule as a function of Mach number.

Mach	NPR	δ_p	$C_{f,g}$	$C_{d,p}$
0.3	3.6	-0.363	0.8730	0.9848
0.7	5.2	-0.244	0.9107	0.9825
0.9	6.0	0.358	0.9331	0.9848
1.2	7.2	0.398	0.9548	0.9852

Table 2. Internal performance for baseline simulations, no secondary fluidic injection.

Mach	NPR	δ_p	$C_{f,e,svs}$	C_d	$C_{d,p}$	$C_{d,s}$
0.05	3.6	-19.46	.9048	.9792	.9843	.8981
0.05	5.2	-14.73	.9357	.9791	.9834	.9101
0.05	6.0	-12.49	.9438	.9785	.9827	.9114
0.05	7.2	-9.94	.9301	.9784	.9824	.9143

Table 3. Internal performance for vectoring simulations with static freestream conditions, $p_{t,s}/p_{t,p}=0.6$.

Mach	NPR	δ_p	$C_{f,e,svs}$	C_d	$C_{d,p}$	$C_{d,s}$
0.3	3.6	-16.69	.8635	.9778	.9825	.9023
0.7	5.2	-11.83	.9249	.9796	.9841	.9084
0.9	6.0	-10.97	.9318	.9783	.9827	.9082
1.2	7.2	-7.76	.9218	.98	.9844	.9094

Table 4. Internal performance for vectoring simulations with the scheduled freestream Mach number, $p_{t,s}/p_{t,p}=0.6$.

M	NPR	δ_p	$C_{f,e,svs}$	C_d	$C_{d,p}$	$C_{d,s}$
0.3	3.6	-16.69	.8635	.9778	.9825	.9023
0.3	7.2	-9.98	.9413	.9770	.9810	.9132
0.3	14.588	-5.27	.9400	.9758	.9798	.9119
1.2	3	-7.84	.8534	.9804	.9880	.8586
1.2	7.2	-7.76	.9218	.9800	.9844	.9094
1.2	14.588	-5.28	.9402	.9786	.9828	.9128

Table 5. Effect of NPR on internal performance for vectoring simulations, $p_{t,s}/p_{t,p}=0.6$.

$p_{t,s}/p_{t,n}$	w_s/w_n	δ_p	$C_{f,e,svs}$	C_d	$C_{d,p}$	$C_{d,s}$
	0.0001	-0.363	.8730	-	.9848	-
0.6	0.058	-16.69	.8635	.9778	.9825	.9023
1	0.965	-13.31	.8794	.9777	.9847	.9107

Table 6. Effect of secondary fluidic injection on internal performance for NPR=3.6 with a freestream M=0.3.
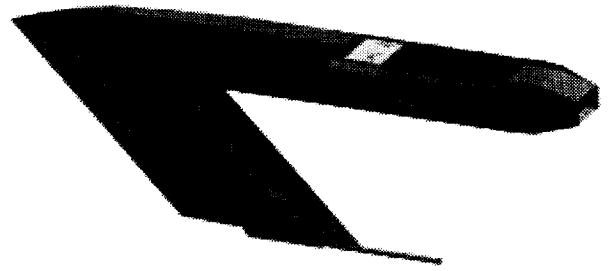
Figure 1. Isolated nacelle mounted on a strut.
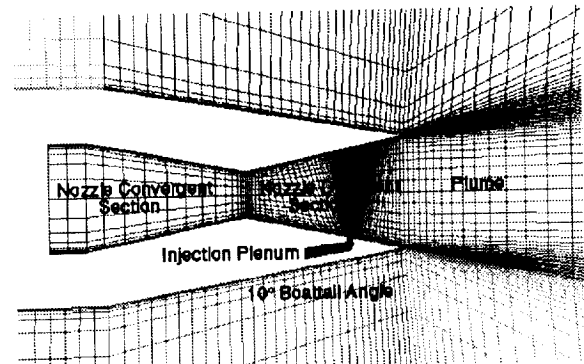
Figure 2. Internal blocking structure.
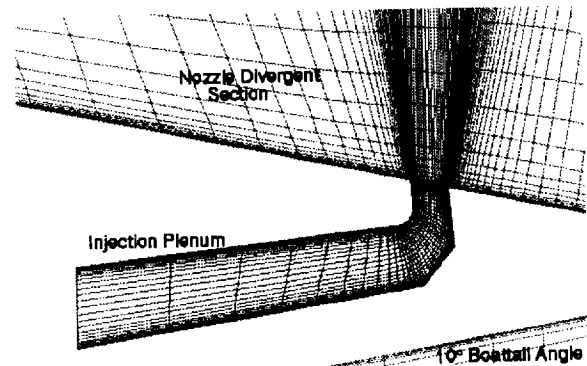
Figure 3. Injection plenum block.
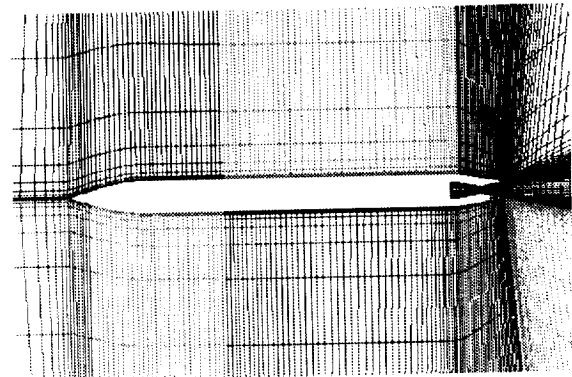
Figure 4. Centerline cut of the isolated nacelle and nozzle.
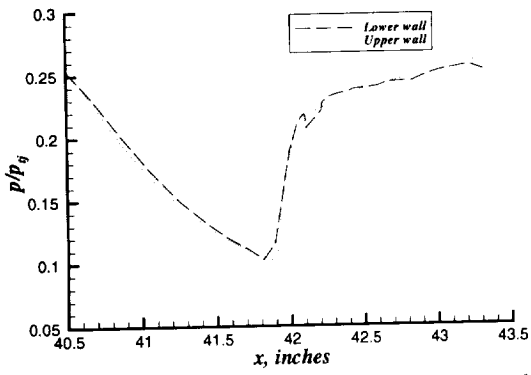
(a) Expanded view of the pressure distributions along the nozzle centerline, divergent walls.
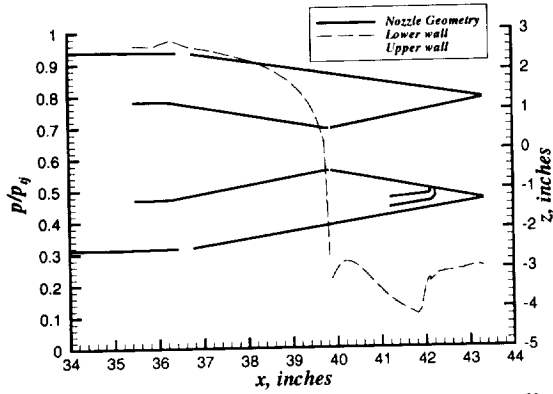
(b) Pressure distributions along the nozzle centerline.
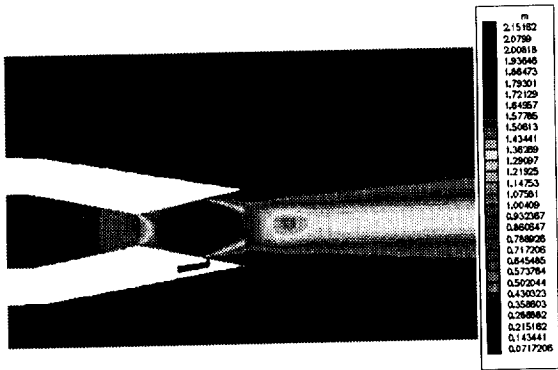
(c) Mach contours along the nozzle centerline.

(d) Reverse flow on divergent wall, u-velocity vectors.

Figure 5. NPR=3.6, *M*=0.3, no injection.
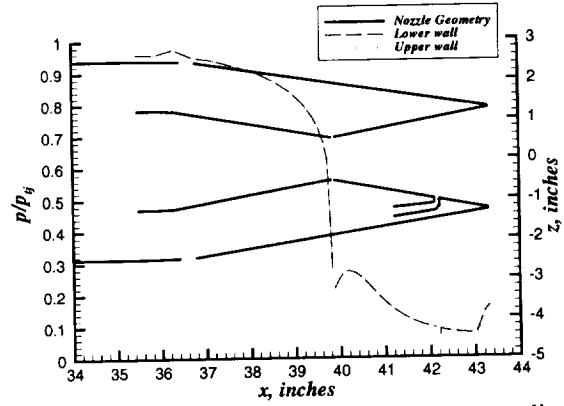
(a) Pressure distributions along the nozzle centerline.
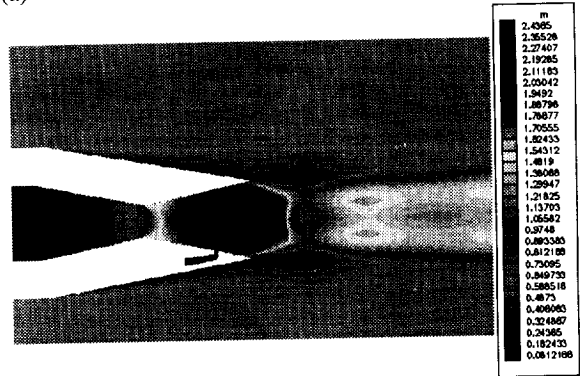
(b) Mach contours along the nozzle centerline.

Figure 6. NPR=5.2, *M*=0.7, no injection.
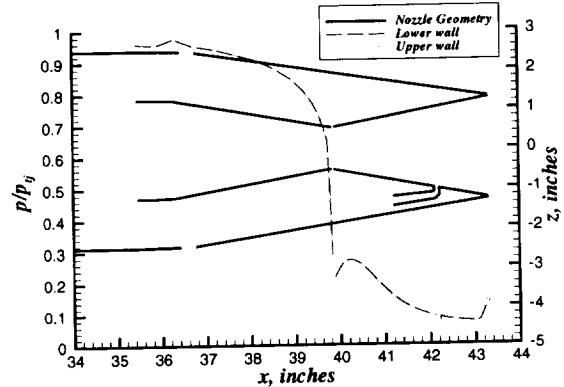
(a) Pressure distributions along the nozzle centerline.
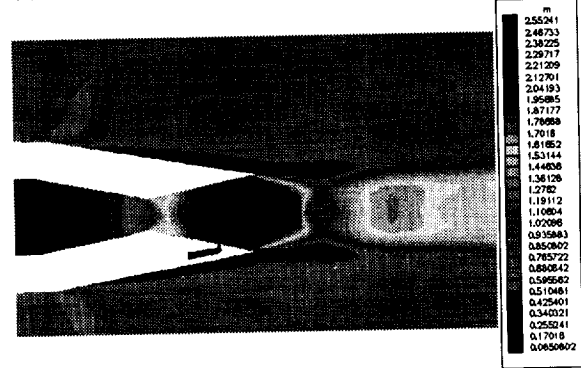
(b) Mach contours along the nozzle centerline.

Figure 7. NPR=6, *M*=0.9, no injection.
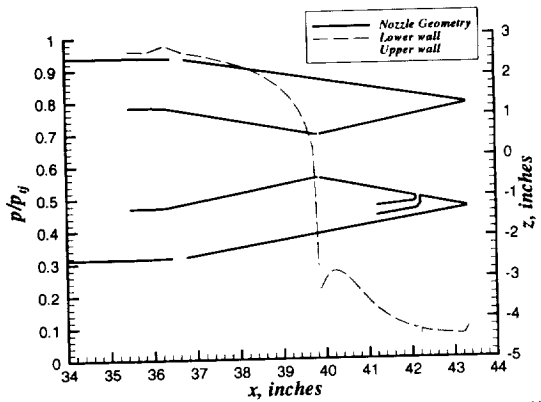
American Institute of Aeronautics and Astronautics

(a) Pressure distributions along the nozzle centerline.
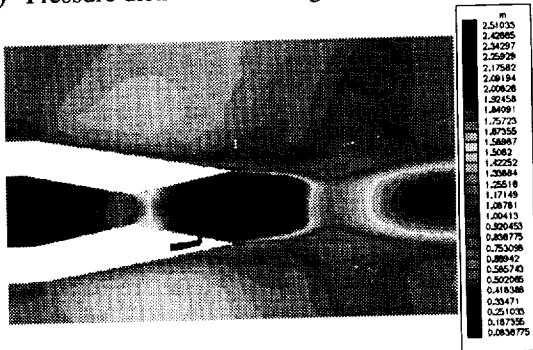
(b) Mach contours along the nozzle centerline.

Figure 8. NPR=7.2, *M*=1.2, no injection.

(a) *M*=0.3 freestream conditions.

(b) Static (*M*=0.05) freestream conditions.

Figure 10. Mach contours along the nozzle centerline, NPR=3.6, $p_{t,s}/p_{t,p}$ =0.6 w_s/w_p =5.8%.
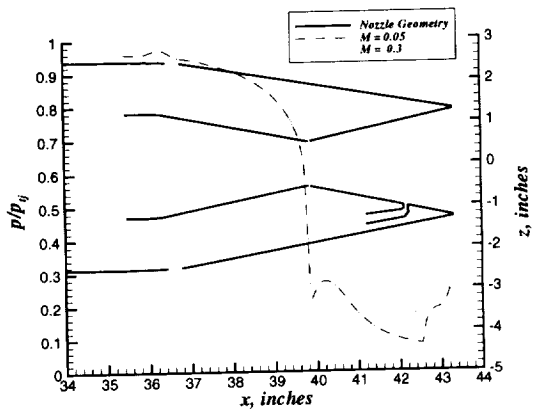

(a) Upper wall
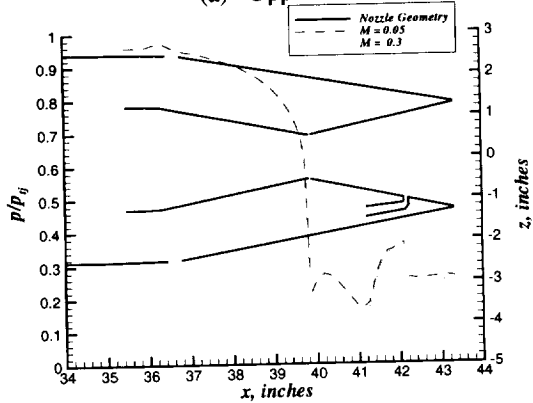
(b) Lower wall

Figure 9. Effect on freestream flow on internal, centerline pressure distributions, NPR=3.6, $p_{t,s}/p_{t,p}$=0.6.
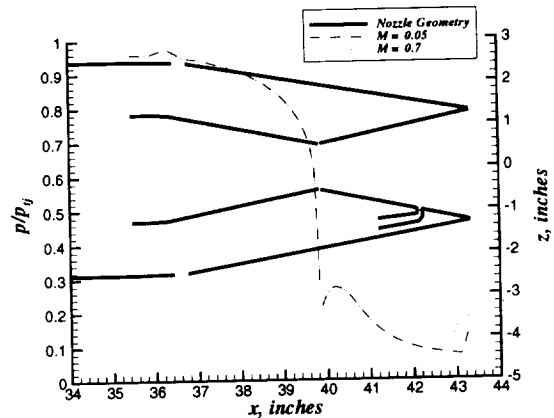

(a) Upper wall
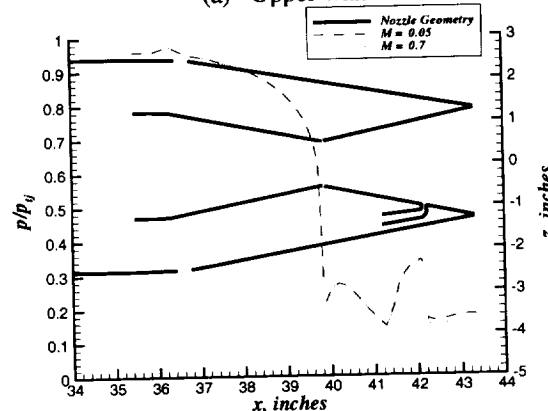
(b) Lower wall

Figure 11. Effect on freestream flow on internal, centerline pressure distributions, NPR=5.2, $p_{t,s}/p_{t,p}$ =0.6.

11

American Institute of Aeronautics and Astronautics
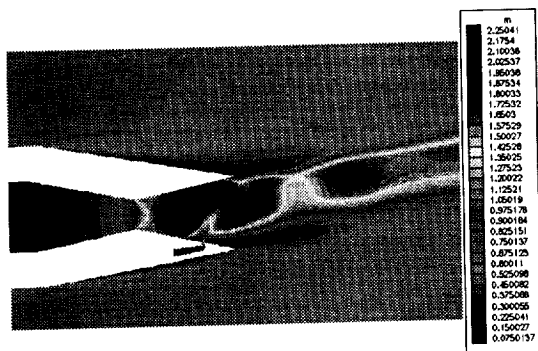
(a) *M*=0.7 freestream conditions.
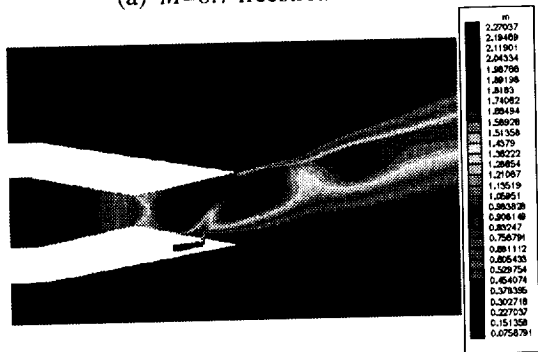
(b) Static (*M*=0.05) freestream conditions.

Figure 12. Mach contours along the nozzle centerline, NPR=5.2, $p_{t,s}/p_{t,p}$ =0.6 w_s/w_p =5.8%.
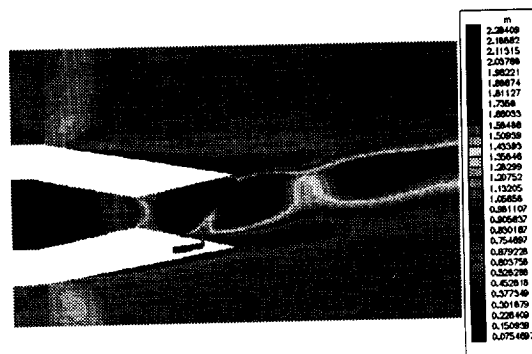
(a) *M*=0.9 freestream conditions.
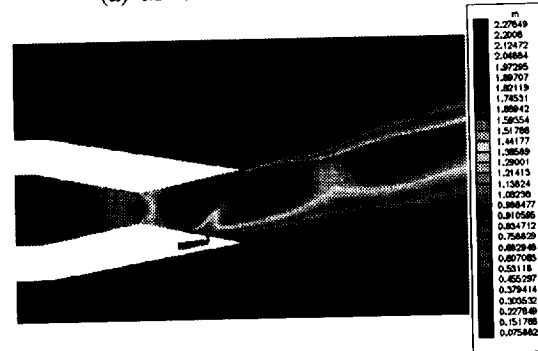
(b) Static (*M*=0.05) freestream conditions.

Figure 14. Flow field comparisons along the nozzle centerline, NPR=6, $p_{t,s}/p_{t,p}$ =0.6 w_s/w_p =5.8%.
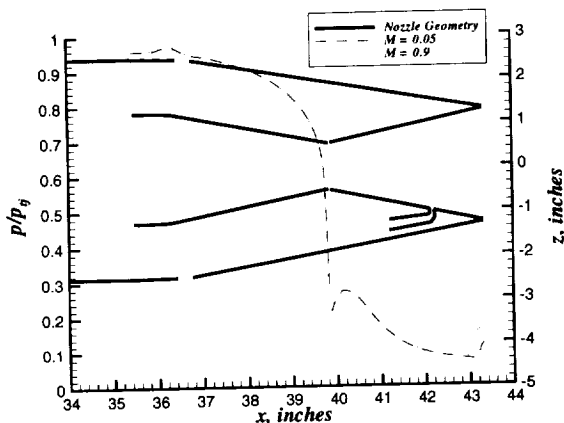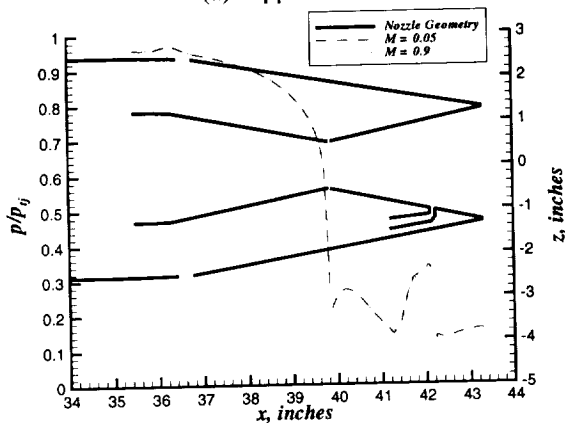

(a) Upper wall

(b) Lower wall

Figure 13. Effect on freestream flow on internal, centerline pressure distributions, NPR=6, $p_{t,s}/p_{t,p}$ =0.6.
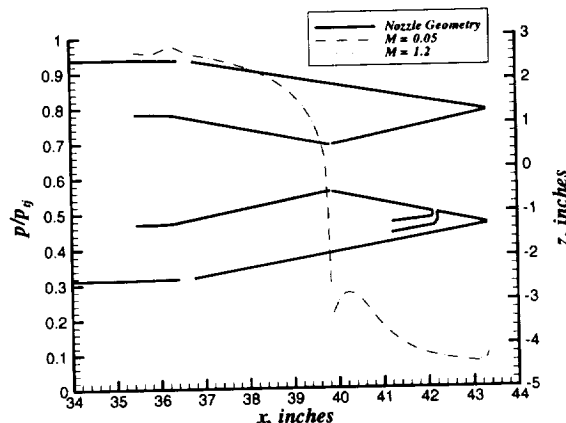
(a) Upper wall
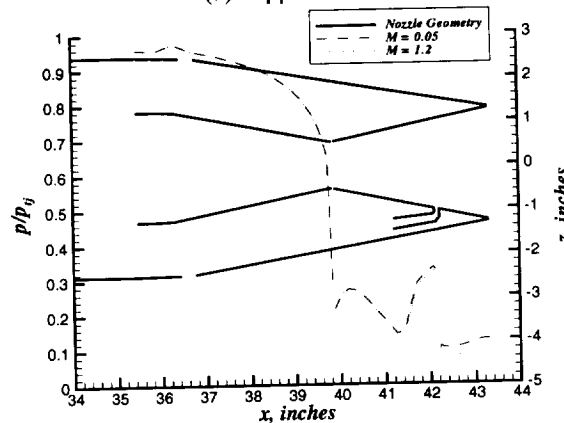
(b) Lower wall

Figure 15. Effect on freestream flow on internal, centerline pressure distributions, NPR=7.2, $p_{t,s}/p_{t,p}$ =0.6.

12
American Institute of Aeronautics and Astronautics
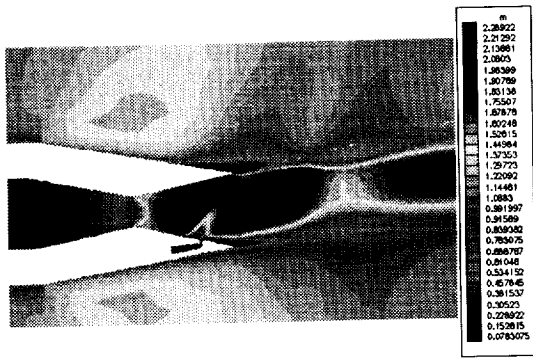
(b) $M=1.2$ freestream conditions.
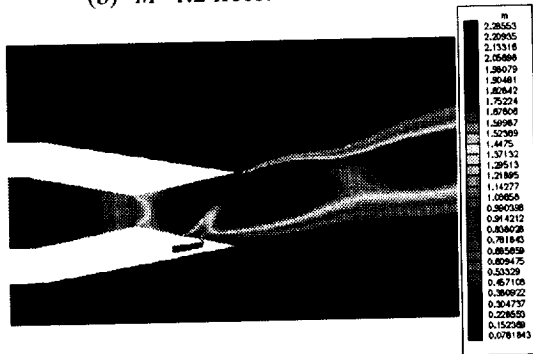
(b) Static ($M=0.05$) freestream conditions.
Figure 16. Flow field comparisons along the nozzle centerline, NPR=7.2, $p_{t,s}/p_{t,p}$ =0.6 w_s/w_p=5.8%.
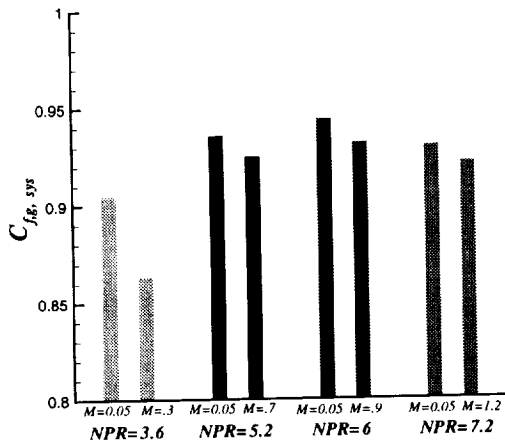
Figure 17. Effect of a freestream flow on gross thrust ratio.
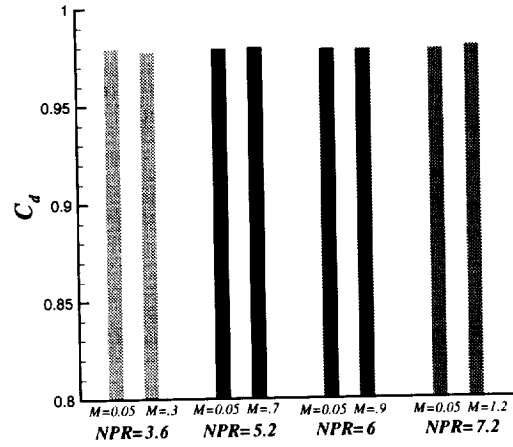

Figure 18. Effect of a freestream flow on discharge coefficient.
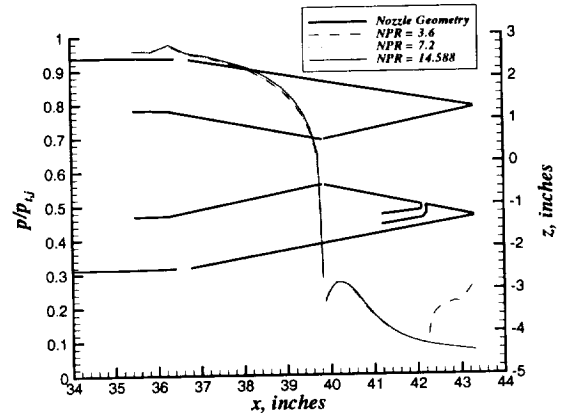
(a) Upper wall
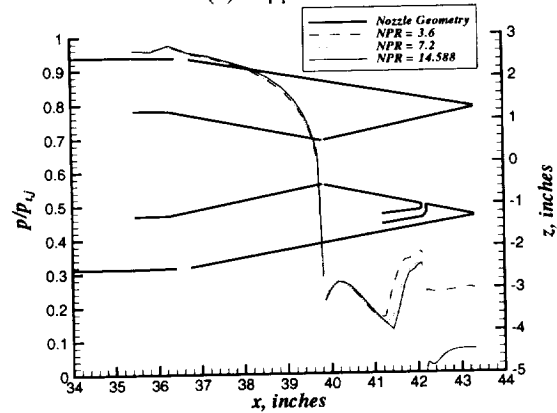
(b) Lower wall

Figure 19. Effect of NPR on internal, centerline pressure distributions with $M=0.3$ freestream conditions.

American Institute of Aeronautics and Astronautics
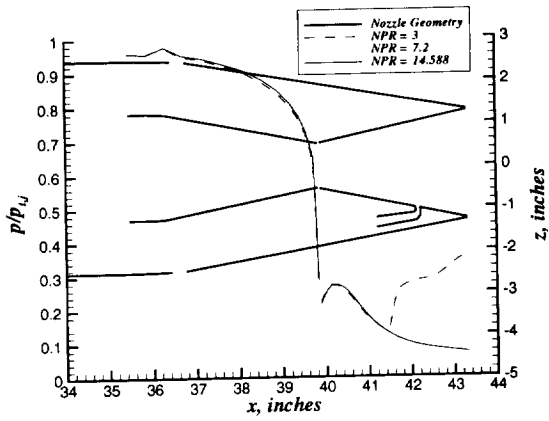
(a) Upper wall

(b) Lower wall

Figure 20. Effect of NPR on internal, centerline pressure distributions with *M*=1.2 freestream conditions.
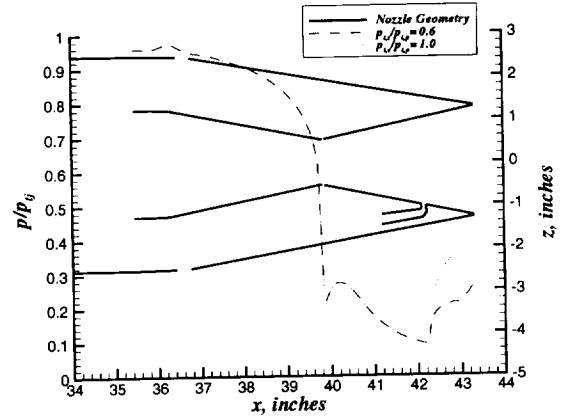

(a) Upper wall
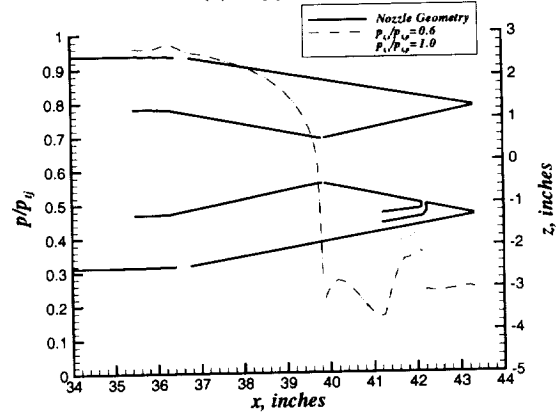
(b) Lower wall

Figure 21. Effect of injection total pressure on internal, centerline pressure distributions for NPR=3.6 with *M*=0.3 freestream conditions.
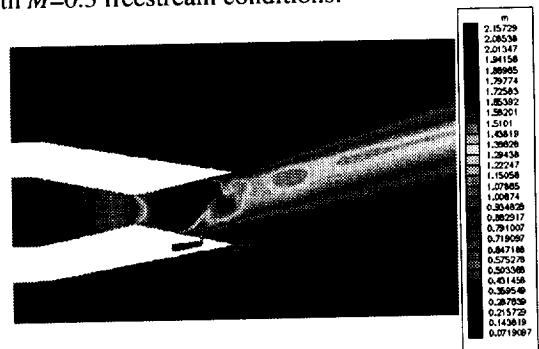
(a) Secondary to primary total pressure ratio of 0.6.
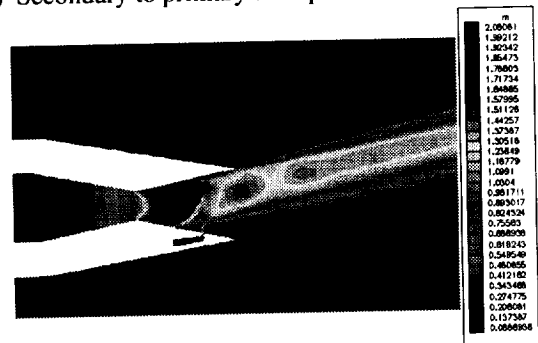
(b) Secondary to primary total pressure ratio of 1.

Figure 22. Effect of injection total pressure on Mach contours for NPR=3.6 with *M*=0.3 freestream conditions.